Preprocessing EO-1 Hyperion hyperspectral data to support the application of agricultural indexes

Article *in* IEEE Transactions on Geoscience and Remote Sensing · July 2003

DOI: 10.1109/TGRS.2003.813206 · Source: IEEE Xplore

5 authors, including:

Tim McVicar
The Commonwealth Scientific and Industrial Research Organisation
218 PUBLICATIONS **10,704** CITATIONS

SEE PROFILE

Thomas G. Van Niel
The Commonwealth Scientific and Industrial Research Organisation
82 PUBLICATIONS **3,839** CITATIONS

SEE PROFILE

David Jupp
The Commonwealth Scientific and Industrial Research Organisation
141 PUBLICATIONS **6,333** CITATIONS

SEE PROFILE

Preprocessing EO-1 Hyperion Hyperspectral Data to Support the Application of Agricultural Indexes

Bisun Datt, Tim R. McVicar, Tom G. Van Niel, David L. B. Jupp, *Associate Member, IEEE,* and Jay S. Pearlman, *Senior Member, IEEE*

***Abstract*—The benefits of Hyperion hyperspectral data to agriculture have been studied at sites in the Coleambally Irrigation Area of Australia. Hyperion can provide effective measures of agricultural performance through the use of established spectral indexes if systematic and random noise is managed. The noise management strategy includes recognition of "bad" pixels, reducing the effects of vertical striping, and compensation for atmospheric effects in the data. It also aims to reduce compounding of these effects by image processing. As the noise structure is different for Hyperion's two spectrometers, noise reduction methods are best applied to each separately. Results show that a local destriping algorithm reduces striping noise without introducing unwanted effects in the image. They also show how data smoothing can clean the data and how careful selection of stable Hyperion bands can minimize residual atmospheric effects following atmospheric correction. Comparing hyperspectral indexes derived from Hyperion with the same indexes derived from ground-measured spectra allowed us to assess some of these impacts on the preprocessing options. It has been concluded that preprocessing, which includes fixing bad and outlier pixels, local destriping, atmospheric correction, and minimum noise fraction smoothing, provides improved results. If these or equivalent preprocessing steps are followed, it is feasible to develop a consistent and standardized time series of data that is compatible with field-scale and airborne measured indexes. Red-edge and leaf chlorophyll indexes based on the preprocessed data are shown to distinguish different levels of stress induced by water restrictions.**

***Index Terms*—Agricultural indexes, Hyperion, hyperspectral, image processing.**

I. Introduction

THE HYPERION sensor [1], carried by the National Aeronautics and Space Administration (NASA) Earth Observing 1 (EO-1) satellite [2], is the first spaceborne hyperspectral instrument to acquire both visible near-infrared [(VNIR) 400–1000 nm] and shortwave infrared [(SWIR) 900–2500 nm] spectra. Hyperion is a pushbroom sensor with two spectrometers and a single telescope. The EO-1 satellite is in a sun-synchronous orbit at 705-km altitude and is nominally 1 min behind the Landsat-7 satellite. Hyperion images 256 pixels with a nominal size of 30 m on the ground over a 7.65-km swath. The platform attitude can vary as the satellite is rolled to image specific targets. During the first year of operation, Hyperion processing was developed and refined to a stage (Level 1B1) where well-calibrated data became routinely available. In this paper, we examine processing and noise reduction methods that can be applied post-Level 1B1 to provide consistent time series of Hyperion data for an agricultural site near Coleambally in New South Wales (NSW), Australia. This will be referred to as the Coleambally Irrigation Area Site (CIAS). The benefits to that study, and the implications for more general agricultural applications, are assessed by focusing on crop attributes that can be derived from Hyperion using a range of hyperspectral indexes.

TABLE I
COMMON SPECTRAL FEATURES FOR CROPS AND SOILS

General Spectral Region (nm)	Indication
400 to 700	PAR region – photosynthetic pigments
680	Chlorophyll absorption
700 to 750	Red Edge (Chlorophyll)
1080 to 1170	Liquid Water Inflection
1700 to 1780	Various Leaf Waxes and Oils
2100	Cellulose
2100 to 2300	Soil properties (clays)
2280 to 2290	Nitrogen / Protein

Hyperion data have three potential advantages over spaceborne multispectral instruments, such as Landsat Enhanced Thematic Mapper (ETM). First, they can provide an enhanced level of information for atmospheric correction to derive surface reflectance. Second, they can provide access to detailed spectral indexes based on surface reflectance. Finally, they can be used to integrate (or "bin") the hyperspectral data consistently to synthetic bands equivalent to any of the broadband sensors or to bands of yet to be developed instruments. This spectral "binning" of Hyperion will be dealt with in a separate paper. This paper investigates the first two advantages and how they benefit from careful preprocessing.

II. Key Spectral Indexes for Agricultural Assessment

The use of broadband space-based remote sensing is well established in agriculture for regional and global monitoring and assessment [3], as is the use of spectrally more detailed information at the laboratory scale [4]. Current research is using airborne and ground-based hyperspectral data [5]–[7] to scale laboratory techniques to remote platforms.

Manuscript received July 22, 2002; revised January 1, 2003. This work was supported by the Commonwealth Scientific and Industrial Research Organization Earth Observation Centre. The work of T. McVicar and T. Van Niel was supported by the Cooperative Research Centre for Sustainable Rice Production under Project 1105. The work of J. Pearlman was supported by the National Aeronautics and Space Administration Earth Observing 1 Program.

B. Datt and D. L. B. Jupp are with the Commonwealth Scientific and Industrial Research Organization Earth Observation Centre, Canberra, ACT 2601, Australia.

T. R. McVicar and T. G. Van Niel are with the Commonwealth Scientific and Industrial Research Organization Land and Water, Canberra, ACT 2601, Australia.

J. S. Pearlman is with the Advanced Network Centric Operations, Phantom Works, Boeing Company, Seattle, WA 98124 USA.

Digital Object Identifier 10.1109/TGRS.2003.813206

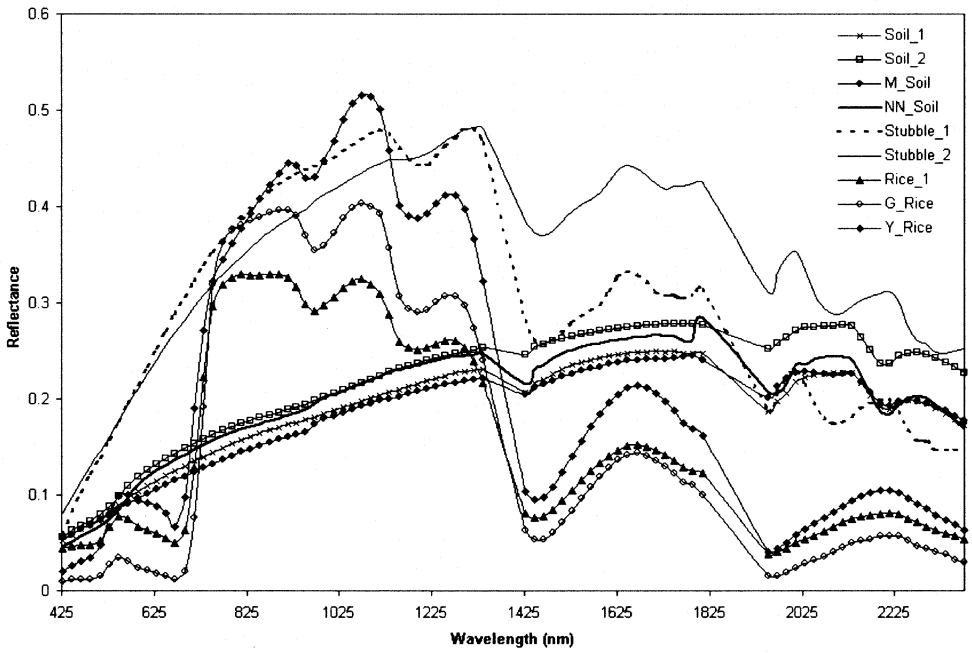

Fig. 1. Typical spectral features occurring in the CIAS. Mean ASD spectra (convolved to 176 Hyperion bands) for the nine sampling sites are shown.

TABLE II
SITES MEASURED BY AN ASD AT CIAS

Site Name	Date	Description	Number of ASD Sites	Start Time	Finish Time
Soil_1	12 Jan	Medium soil clumps	25	0944	1010
Stubble_1	12 Jan	Winter wheat stubble, lightly grazed by sheep.	25	1035	1058
Stubble_2	12 Jan	Winter wheat stubble, heavily grazed by sheep.	25	1125	1146
Soil_2	12 Jan	Large soil clumps	25	1403	1434
M_Soil	13 Jan	Large soil clumps, recently burnt stubble	5	1611	1619
NN_Soil	14 Jan	Tilled field; was to be planted with soybeans, however water restrictions prevented this.	18	1025	1057
Rice_1	14 Jan	Flooded rice (40-90% canopy closure).	12	1218	1418
Y_Rice	14 Jan	De-watered rice, showing obvious signs of water stress.	4	1618	1652
G_Rice	14 Jan	De-watered rice, showing no signs of water stress.	4	1712	1732

The work in progress at the CIAS uses field and laboratory spectral data to calibrate and investigate various derivative and integral indexes. The aim is to find indexes most sensitive to plant nitrogen, water, chlorophyll, lignin, cellulose, and other plant chemical substances plus soil chemical factors such as clay composition and soil nitrogen content. The major such spectral regions are summarized in Table I.

A range of ground spectra with a 1-nm resolution has been taken within the CIAS as validation for Hyperion and as information to accompany site sampling. The site means obtained from data taken by an Analytical Spectral Devices (ASD) Fieldspec spectroradiometer are plotted in Fig. 1 (see Table II). These spectra have been integrated to the 10-nm Hyperion bands for later comparison with Hyperion data and display signatures and spectral features typical of green vegetation, dry vegetation, and soils. A green reflectance peak near 550 nm, photosynthetic chlorophyll absorption (680 nm), a steep slope in the red-edge region (700–750 nm), and leaf water absorption near 970 and 1240 nm are present in the crop spectra. The soil spectra show clay absorption near 2200 nm, and the stubble spectra show lignin/cellulose absorption near 2100 and 2300 nm and plant wax/oil absorption near 1720 nm.

We have selected six indexes to assess the effects of noise management. The wavelengths used in the formulation of these indexes are located within what we will term the "stable" bands of Hyperion (see Section V-C). This provides a reasonable expectation of stable calculation of these indexes. All Hyperion wavelengths reported in this paper are based on the central wavelengths corresponding to pixel 128. The six indexes are defined as follows.

1) *The red-edge (RE) wavelength* is the wavelength position of the maximum slope in the red-near-infrared (700–750 nm) reflectance of vegetation. Several studies have shown that the RE wavelength is correlated with chlorophyll content in leaves and canopies [8]–[10]. The RE wavelength is a good candidate for monitoring vegetation productivity, as well as detecting the onset of stress and senescence. The RE shifts to longer wavelengths during plant growth (increasing chlorophyll content) and to shorter wavelengths during stress (chlorophyll decline in leaves).
2) *The first-derivative value at the red edge (dRE)* defines the value of the maximum slope associated with the RE wavelength above. This index can be sensitive to green vegetation amount [percent cover and leaf area index (LAI)]. Filella and Peñuelas [11] found the area of the red-edge peak to be a strong indicator of LAI. Other variants of dRE using the sum of first and second derivative values around the red-edge band or derivative green vegetation indexes (DGVIs) have also shown strong linear relationships with green vegetation cover [12], [13]. The original Hyperion bands used here to develop both the RE and the dRE were 33 to 40 or wavelengths 681.8–753.0 nm.
3) *A leaf chlorophyll index (LCI)* developed in [14] was found there to be a sensitive indicator of chlorophyll content in leaves and was less affected by scattering from the leaf surface and internal structure variations. LCI is a ratio of relative chlorophyll absorption depths in the RE (710 nm) and red (680 nm) wavelengths. It works best at moderate to high chlorophyll levels. The value of LCI increases as leaf chlorophyll content increases, and is calculated as

$$\mathrm{LCI} = \frac{R_{850} - R_{710}}{R_{850} - R_{680}} \tag{1}$$

where, in [14], R_x = the reflectance at wavelength x = 850, 710, and 680 nm. The same notation applies throughout the paper. The Hyperion band numbers used to develop the LCI here are 50, 36, and 33. These bands correspond to wavelengths of 854.7, 712.3, and 681.8 nm, respectively.
4) *The water index (WI)* compares the leaf (liquid) water absorption band near 970 nm with a reference band at 900 nm, which does not show leaf water absorption [15]. The value of WI increases with leaf water content. WI is calculated as

$$\mathrm{WI} = \frac{R_{900}}{R_{970}}. \tag{2}$$

For Hyperion, bands 55 and 83 were used which correspond to central wavelengths of 905.5 and 973.1 nm, respectively.
5) *The normalized difference water index (NDWI)* is based on a leaf (liquid) water absorption band near 1240 nm and a nonabsorbing reference band near 860 nm [16]. The value of NDWI also increases with leaf water content, and is calculated as

$$\mathrm{NDWI} = \frac{R_{860} - R_{1240}}{R_{860} + R_{1240}}. \tag{3}$$

For Hyperion, bands 51 and 110 were used which correspond to wavelengths of 864.8 and 1245.4 nm, respectively.
6) *The 2200-nm absorption feature [or clay index (CI)]* present in the Coleambally soils results from combinations and overtones of hydroxyl absorption in the clay lattice structure [17]. This feature is present in the reflectance spectrum of kaolinite, a common clay mineral. CI was calculated as the area of the continuum removed reflectance spectrum between 2193 and 2213 nm, and used Hyperion bands 204, 205, and 206 corresponding to wavelengths of 2193.8, 2203.9, and 2214.0 nm. Continuum-removed absorption feature analysis is a useful method for estimating the abundance of compounds from reflectance spectra of samples [18]. The band depth and/or area of the continuum removed absorption features are calibrated against the concentration of chemical compounds of interest or compared with contents of spectral libraries [19], [20]. Such indexes are robust to residual effects following atmospheric correction.

III. Coleambally Irrigation Area Site: Data and Image Base

The CIAS is a 95 000 ha site in southern NSW, Australia (Latitude 34° 48′ 4.3" S, Longitude 146°0′ 48.96" E, 120 m above sea level) that has over 500 farms with large (up to 70 ha) flat uniform fields. The climate has high variability, but the water usage and cropping area are well managed at regional and farm levels. Farming practices are mechanized and intensive, and landholders are interested in maximizing efficiencies through better management.

The CIAS is a focus of remote sensing research to determine the information content available from current broadband and hyperspectral satellite sensors. The CIAS has an excellent base of geographic and agricultural management information plus survey information from specific farms. Since December 2000, a time series of Landsat ETM and coincident EO-1 images have been collected over two southern hemisphere summer growing seasons (2000/2001 and 2001/2002). There have also been a number of field campaigns to collect spectral and ancillary data for calibration and applications research.

The data for the CIAS on January 12, 2002 include Landsat ETM, EO-1 Hyperion and ALI, plus complementary ground (spectral, canopy characteristics, and plant chemistry), airborne (spectral and geometric), and atmospheric data. An ASD Fieldspec spectroradiometer was used to collect ground-based spectra for selected crops and fields. HyMap airborne scanner data [28], covering the 400–2500-nm spectral range in 126 bands, were also acquired for part of the CIAS on January 12, 2002. A CIMEL Electronique CE318–1 instrument was provided by NASA's AERONET Program [21] (AERONET Instrument Number 69) to measure atmospheric characteristics. The application and accuracy of CIMEL and other sun photometers under Australian conditions is discussed in [22]. Every January, Coleambally Irrigation Co-operative Limited acquire a high-resolution (1 : 50 000 scale or 2-m pixel) digital air photo mosaic over the CIAS. This provided an accurate

geographic base for geometric registration of the various image and other data to a common map base.

The conjunction of these datasets and the nature of the area (road network and field layout plus little relief) makes Coleambally an ideal location for 1) geometric and sensor alignment validation, 2) sensor performance validation, 3) sensor intercalibration, 4) atmospheric correction validation, and 5) agricultural applications development. In an initial study addressing Hyperion geometric accuracy, average rms errors were as small as 12.9 and 11.6 m, respectively, in the across and along track directions. Details can be found in [23]. Recent results also confirm that processing by TRW Corporation to Level 1B1 results in excellent VNIR and SWIR coregistration.

The ASD data were measured over nine sites (Table II). At each site, five ASD spectra were averaged, each spectrum being internally averaged 15 times. Times and dates are local (GMT + 1100). The Hyperion image was acquired at 10:59 A.M. on January 12, 2002. The location of each ASD site was obtained from a real-time differential GPS unit. At four of the sites (two soil and two stubble fields), 100 m $\times$ 100 m grids of spectral data were measured to quantify (inter-) calibration and atmospheric correction performance at the Hyperion scale. These sites represent the largest, stable dynamic range in reflectivity within the study area. At the other five sites, less intensive, more opportunistic spatial sampling occurred on the following two days, but with a wider range of agricultural covers being measured to evaluate the performance of indexes and their correlation with crop and soil information. At all sites surface geometry may introduce some variation into the ASD measurements; however, we have not explicitly corrected the ASD data for sun angle variations due to bidirectional reflectance distribution function (BRDF) effects.

IV. Image Processing to Manage Data and Processing Noise

A. Basic Image Processing Approach

Since Hyperion operates from a space platform with consequently modest surface signal levels and full-column atmospheric effects, its data demand careful processing to manage sensor and processing noise. The approach taken here involves selecting bands of greatest value (i.e., the best tradeoff between information content and noise level for the purposes of the application), addressing the vertical striping noise that the VNIR and SWIR arrays display, and managing residual and introduced noise following a standardized atmospheric correction to apparent surface reflectance.

For many forms of data processing such as classification with training sets, minimum noise faction (MNF) [24] or principal component analysis (PCA) [30], and the application of various indexes, it is not necessary to atmospherically correct image data for a single observation. There is also a significant risk in using atmospheric correction, as it tends to amplify noise levels, hence reducing the SNR. However, there are also many situations, which all occur in our work in the CIAS, where it is important to transform hyperspectral data to apparent surface reflectance. These include its use in data normalization for temporal studies, for persistent calibration of indexes and for the direct application of crop models. They also include its utility for directly matching image data to spectral libraries, ground data and to plant chemistry measurements. CIAS field spectra have been compared with pixel values extracted from atmospherically corrected data using packages such as HATCH [25], FLAASH [26], and ACORN (*http://www.aigllc.com/acorn/intro.asp*). The packages have all been found to provide measures of the atmospheric water vapor that agree in magnitude and variance with measurements made by the CIMEL instrument and had generally good agreement with ASD data taken close to the time of the overpass. These results will be reported separately. Since the different packages gave similar results, we have used the FLAASH package, with standard options, as the baseline for the work reported here due to its close integration with the Modtran 4 code development.

TABLE III
Hyperion 176-Band Subset

Array	Bands	Wavelengths (nm)
VNIR	8 to 57	428 to 926
SWIR	79 to 120	933 to 346
	128 to 166	1427 to 1810
	179 to 223	1942 to 2385

B. Hyperion Noise and Implications for Base Processing

The Hyperion VNIR sensor has 70 bands, and the SWIR has 172 bands providing 242 potential bands. A number of the bands were intentionally not illuminated and others (mainly in the overlap region between the two spectrometers) correspond to areas of low sensitivity of the spectrometer materials. Because of this, only 198 bands have been provided in Hyperion Level 1B1 products; the unused bands (1 to 7, 58 to 76, and 225 to 242) are set to zero values by TRW software during the Level 1B1 processing [27].

The Level 1B1 product provided by TRW [27] includes corrections that remove dark current bias effects and correction steps for what are termed "bad" pixels remaining in the 198 bands. The pixel- and band-dependent calibrations have been adjusted over the life of the sensor and represent a well-balanced set of calibrations through effective use of solar, lunar, intersensor, and vicarious methods. Among the 198, there are four remaining bands in the overlap between the two spectrometers. These are VNIR bands 56 (915.7 nm) and 57 (925.9 nm) and SWIR bands 77 (912.5 nm) and 78 (922.6 nm). It is usual to eliminate two of these to obtain 196 unique bands. In the processing reported here, we have selected as the unique 196 the bands 8 to 57 and 79 to 224. This choice was made, since the SWIR band 78 has the higher level of base noise after destriping (described below). This higher base noise level can be confirmed by analysis of the "dark" images provided with Hyperion data.

Atmospheric water vapor bands that absorb almost all of the incident and reflected solar radiation are easily identified by visual inspection of the image data or by atmospheric modeling. Accepting this as a good criterion for band elimination for land surface applications yields the subset of 176 bands listed in Table III.

The wavelengths removed correspond to strong atmospheric water vapor absorption bands between 1356 and 1417 nm, 1820 and 1932 nm, and above 2395 nm. They are commonly removed from ASD or other spectrometer data (including Hymap) taken under natural light conditions. They are not sampled in the spectral ranges selected in the HyMap airborne scanner [28]. For the work presented here, the 176 bands provide the primary input band set for processing and interpretation.

The 176 Hyperion bands still display additional effects that arise from the pushbroom technology. In this paper, the spatial elements of one line of an image will be called "pixels" and are the same as "samples" in other usage. They sample the land surface in the across-track direction. As the pushbroom moves forward, a given pixel creates a "column" of data or an along-track (vertical direction) dataset. Each column in a single band corresponds to a single detector in one of the arrays.

For pushbroom instruments, a poorly calibrated detector in either the VNIR or SWIR arrays will leave a vertical "stripe" in a displayed image band. The most extreme of these (which contain little or no valid data) are identified as "bad" pixels and interpolated in the Level 1B1 processing. In more recent NASA processing [35], these pixels are listed but left unmodified allowing users to select different methods to handle or replace the pixels. Sometimes additional "bad" pixels occur due to infrequent pixel saturation, which makes the correction for sensor "echo" inoperable and at other times the extra "bad" pixels seem to be associated with events in the space environment such as high-energy particles. Fortunately, there are not many "bad" pixels. The current Level 1B1 "bad" pixel list contains about 17 individual pixels out of 242×256 pixels with two cases where a block of bands for a single pixel needs to be fixed. There are also a number of independent detector offsets that reflect the structure and read-out process of the arrays. These are primarily removed in the dark-correction although some effects remain that are significant for dark targets—such as water bodies—but do not affect the indexes being discussed here.

Hyperion also displays pixel pushbroom effects of a less severe but still problematic nature. These are pixels where the data calibration is effectively spatially and possibly temporally varying at scales determined mainly by array structure rather than the earth's surface structure. At one level, a single detector in one of the arrays may have an anomalous calibration. If such pixels have no association with other detectors they will create pixel-level and pixel-independent vertical stripes in the image data. Spatial correlation can come from within-array interactions and may be related to the read-out process. Correlated blocks of stripes seem more prevalent in the SWIR array than the VNIR array.

Hyperion also has low-frequency array effects such as those due to spectral "smile. This can arise from the optical techniques used to spectrally disperse the input imaged "slit" over the detector arrays. It creates a variation in central wavelength and bandwidth across the swath of the sensor—or in a single image line. The spectral "smile" effect is fully described in other papers in this special issue, and while well characterized prior to launch [27], it is the subject of on-going investigations (such as in [33]) to establish whether there have been changes to its form since launch and to handle specific cases where it affects the derived products.

C. Balancing Vertical Stripes in the VNIR and SWIR Arrays

The statistics of the detector arrays can be studied by accumulating mean, variance, minimum, and maximum data for each pixel in each band over the lines of an image. As discussed above, a vertical stripe is said to occur where the statistics indicate that the image information is likely to be valid (that is, the pixel is not "bad") but with significantly modified gain and offset. We are also assuming that such gains and offsets are relatively stable over a collect—but not necessarily between collects. A general approach to removing vertical stripes with these characteristics is then similar to methods used in the past to balance horizontal stripes in mirror scanner images by histogram equalization [29] or to flatten images affected by limb brightening or to balance detectors in airborne pushbroom sensors [34]. That is, histogram moments, such as the means and variances of the columns in each band, are used to balance the statistics of the arrays to those of a reference histogram.

The pixel balancing introduced here is different in that it may be done either "globally" or "locally." In global balancing, the statistical moments of each column are modified to match those for the whole image for each band. In the local approach, reference moments are estimated locally. However, if an affected pixel is quite extreme but not "bad" in the sense defined above, its presence can adversely affect the local statistics. It is, therefore, best to treat such outliers separately in an initial pass. The initial outlier pass used here is local but uses median statistics and thresholds rather than means to identify the pixels to adjust rather than modifying all of the column data to statistics affected by the outliers.

Mathematically, let m_{ik} be the mean of the detector at the ith pixel position for band k and s_{ik} be the corresponding within-column standard deviation over the data sensed as the image is acquired—or on some group of lines in the image. Moreover, let $\overline{m}_{ik}$ and $\overline{s}_{ik}$ be corresponding "reference" values for these moments. The differences between local and global methods and the outlier or general image passes occur in the way the reference values are established.

Formally, the approaches can all be expressed as finding a gain (α_{ik}) and an offset (β_{ik}) for each detector such that the values of the image data for sample i, line j, and band $k(x_{ijk})$ are modified to

$$x'_{ijk} = \alpha_{ik} x_{ijk} + \beta_{ik} \tag{4}$$

where the gain and offset are computed by

$$\begin{aligned} \alpha_{ik} &= \frac{\overline{s}_{ik}}{s_{ik}} \\ \beta_{ik} &= \overline{m}_{ik} - \alpha_{ik} m_{ik}. \end{aligned} \tag{5}$$

That is, generally speaking, the gain setting controls the within-column standard deviation after processing and the offset controls the mean. It follows that if the reference standard deviations are the same as the actual image values, the result is an additive change with no alteration of the within-column standard deviation.

The global method takes the reference mean to be the total image mean and may also take the reference standard deviation to be the whole image within-column standard deviation

$$\begin{aligned} \overline{m}_{ik} &= \overline{m}_k \\ \overline{s}_{ik} &= \overline{s}_k. \end{aligned} \tag{6}$$

The local methods involve either outlier detection and replacement or the use of local smoothing filters. For outlier detection (assuming "bad" pixels have been previously fixed) it is possible to compute

$$\text{test} = \frac{|m_{ik} - l_{\text{med}}(m_{ik})|}{l_{\text{med}}(s_{ik})} \tag{7}$$

where "l_{med}" indicates a local median of selectable neighborhood. Outlier pixels are those where "test" is above a specified threshold. Pixels with anomalous standard deviations are also identified by a similar formula. The outlier destriping is applied as an initial pass to the identified bands using median values as the reference values.

Local destriping proceeds when the outliers have been treated. It uses as reference values

$$\begin{aligned} \overline{m}_{ik} &= l_{\text{mean}}(m_{ik}) \\ \overline{s}_{ik} &= l_{\text{mean}}(s_{ik}). \end{aligned} \tag{8}$$

The notation "l_{mean}" used here indicates a local mean with selectable neighborhood.

Global equalization to remove the striping is mathematically simple but enforces a very severe constraint of uniform column statistics on an image. Gradients in image radiance and distinct patches of different cover types are common in images, and it is therefore, rare for the vertical column statistics of an image to be well balanced across a whole line in the land surface information. An apparent advantage claimed for global equalization has been that it seems to remove low-frequency effects such as those due to spectral "smile." This comes at the cost of changing the spectra as discussed more fully in Section IV-D.

In our experience, the particular choices of method and settings that work best are different for the VNIR and SWIR arrays. They also tend to vary with environmental conditions and between images with distinctly different land covers (such as forests, crops, water and deserts). The CIAS was treated as a single land cover for this study but the local neighborhoods were different in the VNIR and SWIR arrays as discussed in Section IV-D. Other land covers may well need to be stratified.

D. Testing the Effects of Destriping Using the MNF Transform

The effects of destriping and band selection on Hyperion were tested using the MNF transformation [24]. The MNF technique responds to interactions between the spatial structure of the data and that of the noise when the noise has strong spatial structure. This is the case with the image striping. The MNF cannot generally be used to filter out such effects, since they merge with image information but it can illustrate them clearly, as shown in Fig. 2(a) and (b) where the MNF images of the radiance data are shown. The first MNF band has a strong spatial gradient that corresponds to the spectral "smile" in the VNIR array [Fig. 2(a)]. The subsequent MNF bands are soon dominated by vertical striping [Fig. 2(b)].

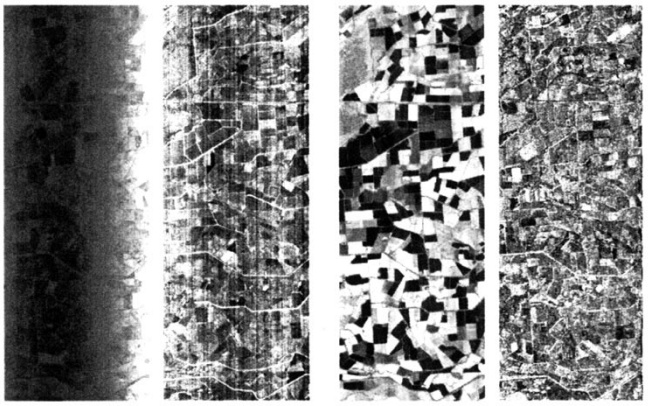

(a) (b) (c) (d)

Fig. 2. MNF Bands 1 and 15 (a) and (b) before and (c) and (d) after global destriping. The 176-band selection from Hyperion was used for the MNF.

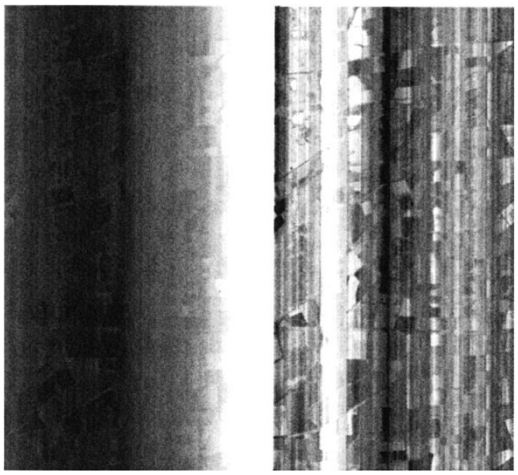

(a) (b)

Fig. 3. MNF bands 1 and 5 of the difference between global destriped and original radiance image. The 176-band selection from Hyperion was used for the MNF.

If global destriping is applied to this image, the result of applying the MNF transformation [Fig. 2(c) and (d)] indicates that both the broad low-frequency effect and the local stripes have been reduced and the image is clean. Moreover, by selecting stable bands that reduce residual atmospheric effects and globally destriping, the MNF becomes clear of the effects noted above to about 20 transformed bands. This is a significant number of features for such data as will be discussed in Section V-B.

However, examination of the differences between the original and destriped data indicates that not only are the pixel to pixel stripes and the broad low-frequency VNIR effect removed, but also midrange frequencies related (in this case) to field sizes and the balance of crop and fallow fields in vertical columns. This is illustrated in Fig. 3 where the MNF Bands 1 and 5 of the differences between the global destriped and raw or "undestriped" radiance images are presented. Removing these field-scale spatial patterns can alter the spectral and spatial characteristics of the data. For example, the predominance of watered rice in one

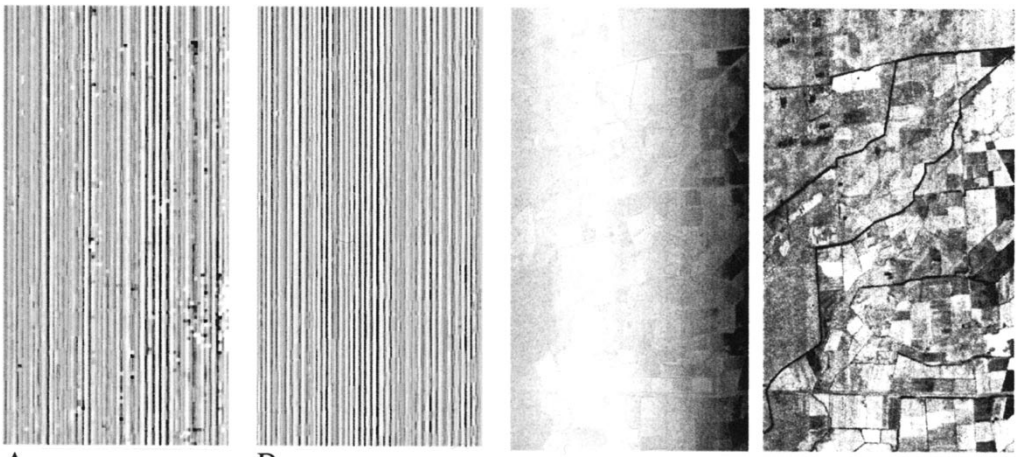

(a) (b) (c) (d)

Fig. 4. MNF bands 1 and 5 of the difference between local destriped and original image. The 176-band selection from Hyperion was used for the MNF.

vertically (north/south) extended area [see Fig. 3(b)] depressed the red region over the whole length of the image to the point where the atmospherically corrected reflectance was negative in the rice fields!

The low-frequency "smile" effect is displayed clearly in the difference image MNF 1 (see [33] for more explanation) while MNF 5 shows a variety of midfrequency effects that are due to fields and not to noise at either the low- or high-frequency end of the scale. These represent informative spatial information that has been removed by the process.

A local method in which the mean and variance used as reference moments were obtained by local averages over five pixels removed pixel-to-pixel scale stripes and not the midfrequency-scale land cover effects. However, it retained the low-frequency "smile" effects in the image data. The result is shown in Fig. 4 where Fig. 4(a) and (b) shows the MNF 1 and 5 for the difference image and Fig. 4(c) and (d) shows the MNF 1 and 15 of the locally destriped bands. The low-frequency "smile" effect is now retained as MNF 1 in the data but the lower order MNF is clear of the local striping and also retains the midfrequency field-scale information.

By examining the statistics of the VNIR and SWIR arrays separately, it is found that the majority of the striping effects in the VNIR are distinct, mainly independent and persistent within and between scenes. They are easily and best removed by a local destriping with a narrow window (such as five pixels). There are also stripes that occur in blocks of pixels and seem to be related to the read-out of the array. These blocks of stripes, which occur more often in the SWIR than the VNIR, are best handled by using a much wider local filter. Local filters with widths of up to 41 pixels were used to reduce these effects in the SWIR in this paper. Block striping in the VNIR seems to be isolated to a few specific bands and these are best treated separately.

With the local approach it is necessary to investigate and understand the nature of the low-frequency pushbroom effects separately from the vertical striping. Global destriping seems to remove the VNIR "smile" effect as well as the stripes but also alters midfrequency spatial effects in the data and so is generally not a good processing step. Local destriping leaves the "smile" effect but only removes pixel-to-pixel scale stripes. Consequently local destriping with different widths in the VNIR and SWIR is the recommended approach in the current application with "smile" being handled in a different way such as has been described in [33].

V. Managing Image Noise Following Atmospheric Correction

Atmospheric correction generally reduces the SNR in the data due to its transfer of the uncorrelated noise to the resulting spectra and also due to the introduction of spectral effects through differences between the model used and the actual atmosphere. The latter includes effects in Hyperion due to spectral "smile" not being taken into account by currently available packages. The management of noise in this situation is dependent on the application, the section of the spectrum of most interest, the environmental conditions during the data acquisition, and many other factors and is currently the focus of continuing research. We have, therefore, used only a few of the known and established steps as examples against which to judge their benefits to agricultural measurements. These are reference spectrum smoothing, MNF smoothing, and band selection.

A. Reference Spectrum Smoothing

The residual noise after atmospheric correction includes two specific types. One is the sensor and processing noise that contributes to the inherent (and reduced) SNR of the data. It is generally uncorrelated spectrally and spatially or has only local correlations that reflect more the geometry of the sensor than the spatial correlations of the scene. The other type includes systematic effects that relate to the differences between the modeled and real atmospheres at the time the data were collected.

In principle, the second could be estimated if you had a range of actual ground surface reflectance values and compared them with the output from the atmospherically corrected data. Systematic and persistent differences may be identified and removed from the image data. Such cleaning actions, based on known spectra, have often been used to improve the results

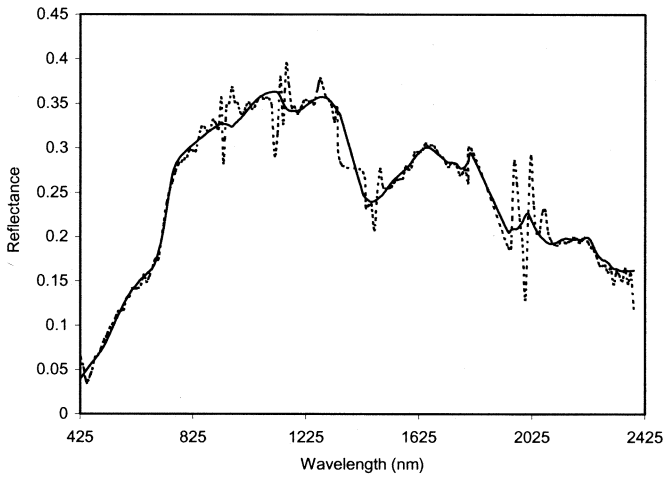

Fig. 5. Mean reflectance spectrum from the Hyperion reflectance image (dashed line) fitted using a linear combination of mean ASD spectra from nine sites (solid line). ASD spectra were integrated to the Hyperion bandpasses.

of atmospheric correction. Since convenient ground spectra of this type are rare in operational data processing, a number of alternative, related approaches have been developed. These are typified by the EFFORT approaches available in ENVI and other packages [31]. In that approach, typical image spectra are obtained and fitted by smooth polynomial or spline functions and the residuals are assumed to be the noise. After that pass, the procedure is much the same as if reference spectra were available.

To provide an example of the general approach for our study—without attempting to define the best operational method—we fitted the overall mean spectrum of the atmospherically corrected Hyperion image by a linear (mixture) combination of the means of the field spectra measured at the nine sites (Fig. 5). In this way, all of the shapes and features that we expected to find in the ASD data were preserved in the fitted model and a global residual noise factor could be defined. The ratio of the mean to the model provides a multiplier to clean up the spectra. This is similar to a directed EFFORT.

B. MNF Smoothing

The uncorrelated, or at most locally spatially correlated, noise is not reduced by a general approach like reference spectrum smoothing. The PCA or MNF transformations are often used for this purpose, as they do not degrade the spatial resolution. The MNF transformation extracts information dimensions relative to an assumed noise structure in the data [24]. The components corresponding to low SNR and unstructured spatial statistics can often be eliminated from the data by "putting the transformation back together" without them—or an "inverse" MNF transformation.

It is useful to have some idea of the significance of the number of transformed bands retained in the data for the inverse MNF transformation. As noted above, global destriping using the 176-band selection seemed to provide about 20 MNF bands that are free of the spatially structured striping noise. A similarly striping-noise free set was obtained after local destriping but with the low-frequency effects retained as

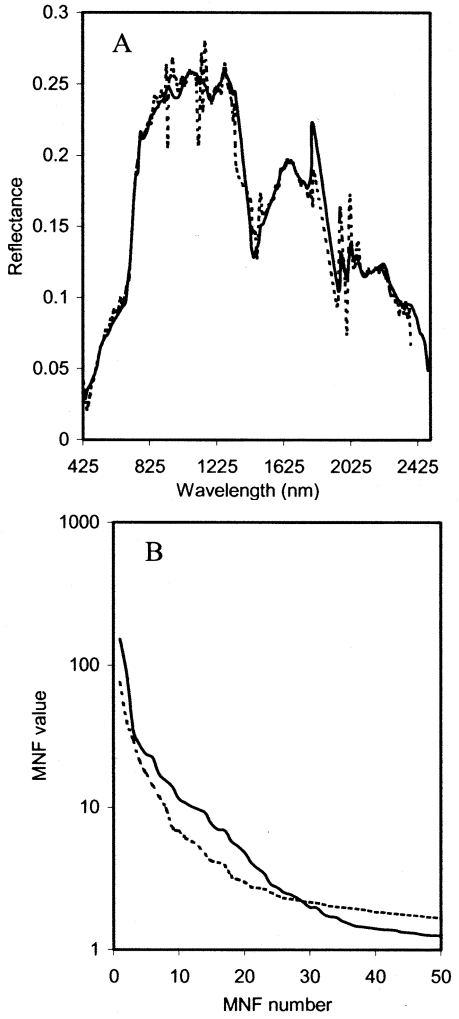

Fig. 6. Hyperion (dashed line) and HyMap (solid line) MNF comparison. (A) Data mean spectra over a common area. (B) MNF values on a Log scale.

high SNR MNF components. However, this provided no basis for assessing the significance of the 20 MNF bands except through visual inspection. To provide a benchmark, MNF of the 126 bands of atmospherically corrected HyMap data [28] acquired at the same time was used for the same area as a coregistered Hyperion data based on the 176-band set. The 176 Hyperion bands cover a similar range to the 126 HyMap bands but with a finer spectral resolution—10 nm compared with 15 nm full-width half-maximum and spacing. The atmospheric correction for the two datasets used the same basic parameters except for the flying height and other platform-dependent settings.

Fig. 6(A) shows the total image means in the common area imaged by both Hyperion and HyMap. The greater level of residual noise visible in the Hyperion mean plot is higher than can simply be ascribed to the narrower bandwidth. With advantages of broader bands, higher signal levels and higher intrinsic SNR, the HyMap data seems to achieve 25 to 30 significant MNF bands [Fig. 6(B)]. Taking 25 to 30 HyMap MNFs as a base potential for resolving MNFs (i.e., the limit of environmental SNR in this application) it is a good achievement to remove noise to achieve 20 MNFs from Hyperion data. The similarity between the HyMap data in Fig. 6(A) and the model

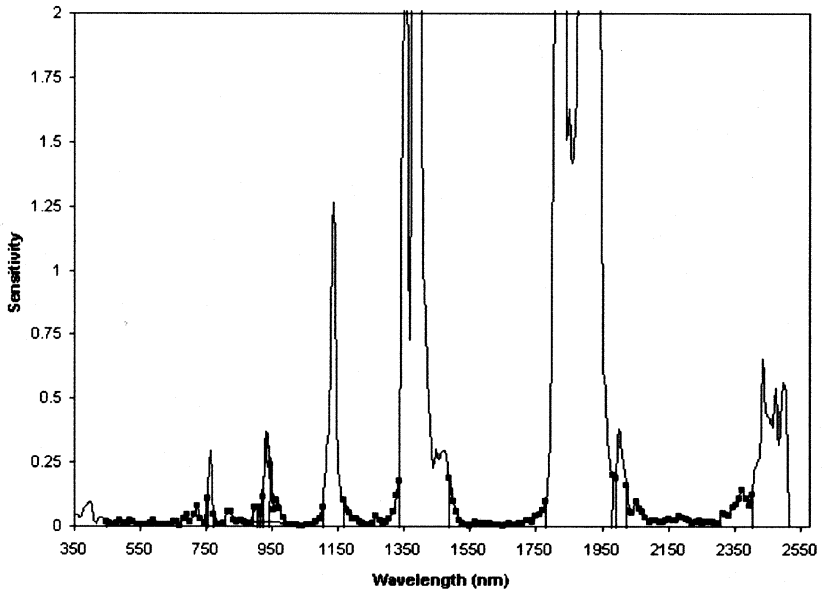

Fig. 7. Estimated sensitivity measure of radiances to changes in location of atmospheric features or Hyperion band centers. Continuous line is the measure and the blocks are the 155 bands selected for "stability."

based on fitted site spectra in Fig. 5 supports the assumption of low residual noise in the HyMap data.

To apply the dimensional noise reduction in practice, it is best to handle the VNIR and SWIR data separately and combine them after the processing. In the following examples, for the inverse MNF transformation we used 12 components in the VNIR and eight in the SWIR. These choices allowed rejection of some low SNR residual array effects and were more conservative than the 20 MNFs from the combined set that were used in the comparison with HyMap. Handling the VNIR and SWIR data separately provides greater capacity to manage the noise due to its different structure in the two arrays.

C. Band Selections That Avoid Residual Atmospheric Noise Effects

The residual noise introduced by atmospheric correction can be reduced by methods such as those described above. However, an alternative or complementary approach is to eliminate bands that are most likely to contain unstable atmospheric artifacts above a certain threshold.

To quantify the choice, an index of band sensitivity to atmospheric effects (such as variations in absorber profile as well as interactions with the sensor) was defined by using the derivative of model radiance as a function of wavelength. In effect, this measure is most sensitive to locations where a change in band center will create the largest differences in radiance. Specifically, atmospheric models were computed for the CIAS based on a clear day as the base and with variations in aerosol and water vapor to provide the range. These were combined with an average surface reflectance computed with a wavelength (λ) step of 1 nm and converted to radiance (L) at the sensor.

Numerical differentiation was used to compute the quantity

$$\text{Sensit} = \left| \frac{\partial \log L}{\partial \lambda} \right|. \tag{9}$$

TABLE IV
155 STABLE HYPERION BANDS

Region	Band Number	Wavelength (nm)
VNIR	10 to 57	447.9 to 925.9
SWIR	81 to 97	952.9 to 1114.3
	101 to 119	1154.7 to 1336.2
	134 to 164	1487.6 to 1790.2
	182 to 221	1971.8 to 2365.2

The results were averaged over the cases of varying atmospheric levels of water vapor and aerosol and then integrated over the Hyperion band passes. The result obtained is partly a function of the conditions at the site and the time of overpass up to the variation introduced by the varying atmospheric data. The final value is plotted in Fig. 7.

There was a level of arbitrariness about the overall level chosen to indicate instability. Initially, a value of 0.25 was selected and then some bands at the edge of atmospheric features were added where there were some important known features to pursue beneath the image noise. Based on this index, a subset of 155 bands (plotted in Fig. 7) has been used as a set of "stable" bands with respect to residual atmospheric feature effects and used to develop indexes and measurements that are free of the effects they create. Table IV presents the resulting choices by original band number and wavelength.

These bands are clearly located in the middle of atmospheric windows and also cover the areas of response of the ETM and ALI band passes, and thus the selection retains the ability to construct intersensor comparisons. Obviously there can be modifications for specific purposes but in most cases we are finding that using these 155 bands provides a simple but effective processing step that avoids, rather than reduces, residual noise. All the indexes used in Section VI used selections from the stable 155 Hyperion bands. However, Fig. 7 also shows that the RE indexes may need special attention.

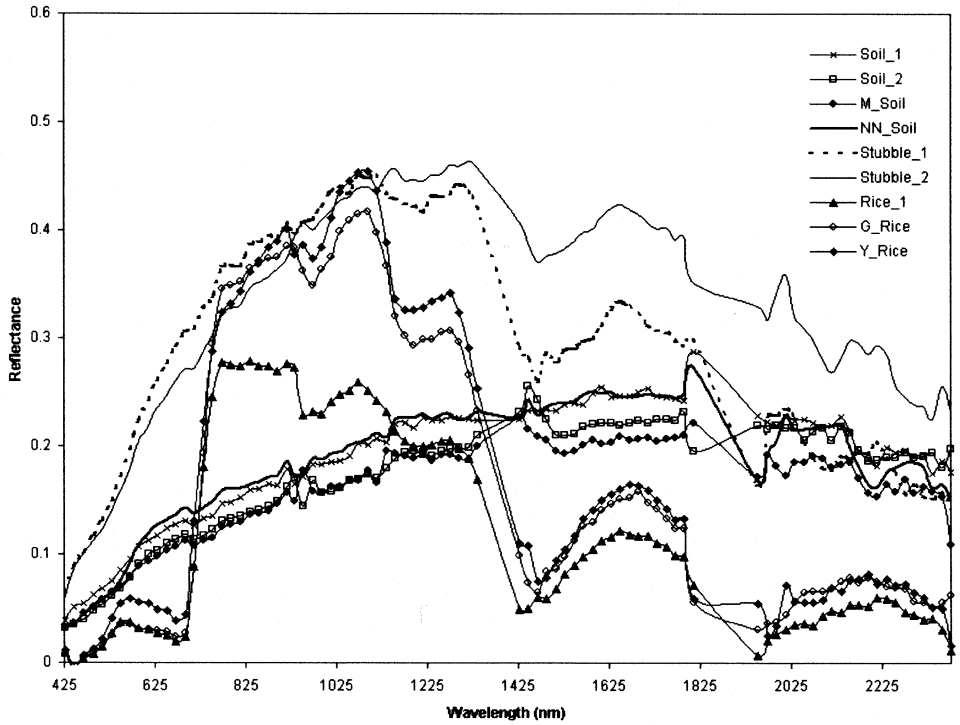

Fig. 8. Mean January 12 Hyperion spectra for the nine sampling sites of Fig. 1. The within-site variation is used to evaluate the indexes.

VI. Agricultural Applications: Measurements From a Space Platform

The benefits of noise management, including the destriping and smoothing operations, were evaluated by comparing the values of selected spectral indexes from the geolocated ASD measurements with values from corresponding Hyperion pixels (Section VI-A). These data do not provide a complete design for the effects discussed (and other effects not fully discussed in this paper such as the "smile" and surface BRDF) but do provide important insights. The mean Hyperion reflectance spectra corresponding to the nine ASD site means of Fig. 1 are shown in Fig. 8. These Hyperion spectra show similar reflectance amplitude and spectral features to the ASD spectra of Fig. 1 but with more noise. The numbers of samples involved in these means varies from site to site and are provided in Table II.

The purpose of the analysis is twofold. First, it is important to know if the information measured using field spectrometry can be retrieved from space data, and second, which noise management strategies increase the consistency between the datasets? The dataset can partly answer these questions, but it is important to keep both its strengths and limitations in mind during the analysis.

The data were obtained at a variety of sites on and during days following the EO-1 overpass on January 12, 2002 (see Section III). To provide a consistent comparison, the ASD spectra were convolved to equivalent Hyperion bands. The sites were chosen to represent different covers, yet were relatively close together for logistical reasons. Being near the center of the Hyperion image the variations due to spectral "smile" are small and so effects due to the "smile" cannot be assessed using these data. The "smile" is better addressed by comparing Hyperion and HyMap data over the common area of the CIAS, and this is reported in [33]. Also, since the most obvious VNIR striping occurs toward the western side of the image, there was little or no visible VNIR striping near the sites. However, the ubiquitous SWIR vertical striping was present everywhere in the image.

For completeness, the comparisons were made on Hyperion images processed in nine ways. First, atmospheric correction, using FLAASH, was applied to the original and globally and locally destriped (Section IV-C) radiance images. These are denoted as 1) Undestriped, 2) Global destriped, and 3) Local destriped. Using these three atmospherically corrected images as inputs to an "MNF-inverse MNF" transformation (using 12 MNFs for the VNIR and eight for the SWIR as described in Section V-B) to smooth the data produced 4) Undestriped MNF smoothing (MNFS), 5) Global destriped MNFS, and 6) Local destriped MNFS. Again the outputs (1)–(3) were used as inputs to the reference spectrum smoothing (RSS) technique (introduced in Section V-A) to create 7) Undestriped RSS, 8) Global destriped RSS, and 9) Local destriped RSS.

Following this, the sensitivity of spectral indexes to crop stress was used as a test of application by comparing Hyperion and ASD derived values for two rice bays known to have different levels of water stress (Section VI-B) from field work and landholder survey.

A. Narrowband Indexes: Performance and Stability

The six indexes introduced in Section II were used to investigate the relationship between the ASD and Hyperion data. In the VNIR region, three were explored: 1) RE, 2) dRE, and 3) LCI. In the SWIR region the clay hydroxyl absorption feature in soils near 2200 nm was selected. In the VNIR/SWIR region, the two leaf water content indexes WI and NDWI were used.

TABLE V
SUMMARY STATISTICS R^2, F-TEST PROBABILITY (P), MEAN (Mn), AND STANDARD DEVIATION (Std) FOR SIX INDEXES FOR HYPERION PREPROCESSED USING NINE OPTIONS. Mn AND Std ARE ALSO GIVEN FOR ASD

Index Name ASD Mn (ASD Std)	RE (nm) 726.97 (2.71)		dRE (μm^{-1}) 42850 (10420)		LCI 0.73 (0.06)		Clay Index 0.039 (0.012)		WI 1.10 (0.07)		NDWI 0.10 (0.05)	
	R^2 (P)	Mn (Std)	R^2 (P)	Mn (Std)	R^2 (P)	Mn (Std)	R^2 (P)	Mn (Std)	R^2 (P)	Mn (Std)	R^2 (P)	Mn (Std)
1 Un-destriped	0.615 (0.008)	727.44 (1.53)	0.350 (0.000)	39187 (3963)	0.681 (0.009)	0.76 (0.04)	0.070 (0.00)	0.053 (0.037)	0.009 (0.325)	1.07 (0.07)	0.123 (0.399)	0.14 (0.05)
2 Global destriped	0.563 (0.003)	727.55 (1.39)	0.241 (0.012)	38495 (6114)	0.581 (0.003)	0.76 (0.03)	0.152 (0.00)	0.060 (0.042)	0.001 (0.137)	1.06 (0.06)	0.098 (0.019)	0.13 (0.03)
3 Local destriped	0.619 (0.007)	727.42 (1.50)	0.353 (0.000)	39197 (4012)	0.680 (0.007)	0.76 (0.04)	0.112 (0.00)	0.051 (0.038)	0.002 (0.324)	1.07 (0.07)	0.122 (0.408)	0.14 (0.05)
4 Un-destriped_MNFS	0.623 (0.006)	727.40 (1.48)	0.355 (0.000)	39133 (3885)	0.687 (0.009)	0.76 (0.04)	0.576 (0.014)	0.028 (0.009)	0.010 (0.457)	1.06 (0.07)	0.154 (0.190)	0.14 (0.04)
5 Global destriped_MNFS	0.563 (0.002)	727.54 (1.35)	0.233 (0.013)	38563 (6119)	0.586 (0.003)	0.76 (0.03)	0.633 (0.240)	0.039 (0.011)	0.004 (0.228)	1.05 (0.06)	0.158 (0.054)	0.13 (0.04)
6 Local destriped_MNFS	0.639 (0.004)	727.37 (1.45)	0.355 (0.000)	39147 (3961)	0.683 (0.007)	0.76 (0.04)	0.622 (0.284)	0.034 (0.013)	0.008 (0.407)	1.07 (0.08)	0.164 (0.433)	0.15 (0.05)
7 Un-destriped_RSS	0.574 (0.006)	728.19 (1.49)	0.349 (0.000)	40065 (4070)	0.682 (0.013)	0.75 (0.04)	0.064 (0.00)	0.061 (0.039)	0.009 (0.425)	1.14 (0.07)	0.123 (0.405)	0.13 (0.05)
8 Global destriped_RSS	0.524 (0.001)	728.34 (1.30)	0.240 (0.016)	39348 (6253)	0.582 (0.005)	0.75 (0.03)	0.147 (0.00)	0.069 (0.043)	0.001 (0.203)	1.13 (0.06)	0.098 (0.020)	0.11 (0.03)
9 Local destriped_RSS	0.580 (0.005)	728.19 (1.47)	0.352 (0.000)	40081 (4119)	0.682 (0.013)	0.75 (0.04)	0.108 (0.00)	0.060 (0.038)	0.002 (0.424)	1.13 (0.07)	0.122 (0.414)	0.13 (0.05)

Indexes from VNIR, SWIR, and combined VNIR/SWIR spectral regions are needed to provide tests for noise reduction due to the different noise statistics in data acquired by Hyperion's two spectrometers. The performance of all six indexes is, however, expected to be relatively stable, since the wavelengths used in their formulation all lie within the 155 "stable" bands we defined for Hyperion.

1) VNIR Indexes: The RE and dRE values were calculated from Hyperion by fitting a third-order polynomial and returning the wavelength and first-derivative value at the inflection point using a generic IDL_ENVI module developed by the CSIRO Division of Exploration and Mining, Mineral Mapping Technologies Group.

The indexes were calculated at the 20 sites for rice (Rice_1, Y_Rice, and G_Rice in Table II) using geolocated ASD spectra and the corresponding georeferenced Hyperion pixels from the reflectance images. The ASD and Hyperion derived index values were compared using linear regression. Summary statistics are provided in Table V.

In most cases (the dRE excepted), the Hyperion values correlate to a good level with ground-based ASD values. This is an encouraging result, since one objective is to use ground-based models or calibrations with the Hyperion data. The dRE is the index most affected by the Hyperion "smile" and this is taken up separately in [33].

The local destriping, MNFS and RSS smoothing all produced similar R^2 values to that of the undestriped image. This is to be expected, as the VNIR SNR is high, and there was no major VNIR vertical striping in the central region of the Hyperion image. However, it is significant that the lowest R^2 values for each index were obtained for the global destriped images (cases 2, 5, and 8 in Table V). This is consistent with the findings in Section VI-A, that global destriping alters the data.

It is important to keep in mind the number of samples involved in these comparisons (20 in this case) as well as the relative standard deviations of the image and ASD data. The sampling strategy at the CIAS for the soil and stubble sites acquired on January 12, 2002 was designed to enable scaling to Hyperion pixels. However, the rice sampling was less intensive and includes more spatial variation (and hence higher standard deviation) due to the scale difference between site and Hyperion data.

2) SWIR Clay Index: CI values were calculated from 55 geolocated ASD spectra of soils (Soil_1, Soil_2, NN_Soil, and M_Soil in Table II) and from the 55 georeferenced Hyperion pixels. Where ASD data fell into the same pixel the values were averaged, there are 55 unique Hyperion pixels associated with the 73 ASD soil measurement sites presented in Table II. The ASD and Hyperion index values were compared using linear regression (Table V). The results in Table V show that both global and local destriping (cases 2 and 3) slightly increased the R^2 values compared to the undestriped image (case 1). Since the region used is in the "stable" area of the SWIR, Hyperion bands 204, 205, and 206 used in the Clay Index did not show heavy striping in the radiance data; thus, the impact of destriping was not large and would be more significant for other SWIR bands.

The largest increase in R^2 was observed with MNF smoothing, as shown for cases 4, 5, and 6 in Table V. This result indicates that base noise has a major impact in the SWIR region compared with stripes and that MNF smoothing reduces this. In this case, as discussed in Section V-B, the MNF smoothing in which the VNIR and SWIR are handled separately is also removing residual array effects. The RSS smoothing (cases 7, 8, and 9 in Table V) did not show any change in R^2 for this index as may be expected from Figs. 5 and 6 and from the way the index is defined. Note that in the best results the means and standard deviations of image and ASD data are similar as would be expected due to the design of the sampling at the soil sites that aimed to bring the data to the same spatial scale.

3) VNIR–SWIR Indexes: The values of WI and NDWI were calculated from 20 geolocated ASD spectra of rice (Rice_1, Y_Rice, and G_Rice in Table II) and from the 20 georeferenced

TABLE VI
MEANS AND STANDARD DEVIATIONS OF RE, LCI, dRE, WI, AND NDWI FOR HYPERION AND ASD MEASUREMENTS IN THE UPPER (WATER STRESSED), AND LOWER (NON-WATER STRESSED) BAYS

Spectral Index	Sensor	Upper Bay	Lower Bay
RE (nm)	Hyperion	726.6 (0.2)	730.3 (0.6)
	ASD	723.6 (1.1)	730.0 (0.5)
LCI	Hyperion	0.73 (0.01)	0.83 (0.02)
	ASD	0.66 (0.02)	0.83 (0.01)
dRE	Hyperion	39441 (688)	44758 (2605)
	ASD	33420 (5713)	54506 (5814)
WI	Hyperion	1.01 (0.04)	1.05 (0.04)
	ASD	1.04 (0.01)	1.12 (0.04)
NDWI	Hyperion	0.08 (0.01)	0.12 (0.02)
	ASD	0.02 (0.01)	0.13 (0.02)

Hyperion pixels. The ASD- and Hyperion-derived index values were then compared using linear regression (see Table V for statistics from WI and NDWI indexes, respectively).

As can be seen from Table V, the R^2 values were nearly zero for most cases. The reason for the low values is almost certainly the low range of variation in the WI and NDWI values for the 20 ASD rice samples. This is shown by the image and site standard deviations. The influence of atmospheric water vapor in the 973- and 1245-nm Hyperion bands was expected to create variation but does not seem to have done so. Relatively few conclusions on the effects of various processing options can be drawn for these two indexes except to note that the absolute values obtained from the ASD spectra and the image are very close. To assess whether the variations are as well related as the means requires a dataset with more underlying variation.

B. Mapping the Onset of Stress Due to Water Restrictions

The images processed in the best of the selections discussed above were then used in a simple but very useful mapping application. Due to reduced water allocations and high water demands in the early growing season, some growers reduced or stopped irrigation much earlier than normal. Irrigation to one of the rice fields (Farm 51, field H) was stopped ten weeks earlier on December 28, 2001. For this "dewatered" field, water was managed by directing water from three bays at the same elevation to the fourth bay at a lower elevation. The landholder attempted to grow a successful crop in the lower bay by directing water from the other bays.

Due to this management strategy, the lower bay was less stressed than the upper bays on January 12, 2002. Geolocated ASD spectra were acquired in the lower (greener, labeled G_Rice) bay and in one of the upper (yellower, labeled Y_Rice) bays on January 14, 2002. Since water stress is associated with a decline in chlorophyll, it would seem possible to use hyperspectral indexes to map the variation. The question is how well can such mapping be undertaken at a regional scale from the EO-1 space platform? Mean and standard deviations of four representative pixels at which geolocated ASD (see G_Rice and Y_Rice in Table II) and georeferenced Hyperion derived values were extracted for the suite of indexes are presented in Table VI for the upper bay (water stressed) and the lower bay (not water stressed).

Despite the restricted statistics, the differences in chlorophyll content between the two bays are captured by the RE and LCI indexes in the Hyperion data. The lower bay with higher chlorophyll content shows significantly higher RE and LCI values compared with the upper bay. Chlorophyll measurements were taken with a Minolta SPAD-502 meter (produced by the Soil-Plant Analysis Development (SPAD) Division, Minolta Camera Company, Osaka, Japan). On January 14, the lower bay had an average of 43.89 (SD $= 3.68$ for four sample locations), and the upper bay had an average of 17.00 (SD $= 2.49$ for four sample locations). At each of the eight locations (four in the upper bay and four in the lower bay) 30 individual "SPAD" measurements were made. The SPAD data are in relative units that are known to be highly correlated with leaf nitrogen concentration.

For RE and LCI indexes, Hyperion and ASD show similar values and trends between the bays. There was close agreement between ASD and Hyperion values in the lower bay, which had a uniform green rice canopy. For the upper bay, Hyperion values were higher than the ASD values, mainly due to the heterogeneous mix of green rice and yellow senescing weeds and the greater spatial averaging in the Hyperion signal. The dRE values were higher for the lower bay in both ASD and Hyperion measurements. This relates to the higher green leaf cover and density in the lower bay compared to the upper bay which had more senescing weeds in it and therefore lower dRE values. However, as in the previous examples, the dRE in the space data has a reduced variation in response than in the ASD values—despite the fact that the ASD data are integrated to Hyperion bands. The NDWI and WI values in the lower bay, for both the Hyperion and ASD data, were higher than the values for the upper bay indicating consistently greater leaf water content in the greener canopy.

On the basis of these results, it appears that one or a number of these indexes taken together could provide useful maps of the state of water stress at the time of the EO-1 overpass. If the stress were to become more severe, it may be expected that the leaf water indexes would become more informative and if the stress progressed to senescence it may be expected that indexes not used here but based on the leaf waxes and oils and cellulose features (see Table I) would track the progression into that stage. These tools are, therefore, ready for analyzing hyperspectral time series as acquired for CIAS.

VII. CONCLUSION

The consistency and degree of relationship among the indexes derived from the space platform and those from field data provide the entry point to intercalibration between laboratory, ground-based, airborne, and spaceborne data. However, the results from this research indicate that preprocessing including band, or feature, selection, atmospheric correction, local destriping, and noise management such as that provided by minimum noise fraction smoothing were needed to achieve this.

Destriping is an area of current focus and development for Hyperion data processing. The work reported here supports the use of local methods to remove the stripes with the degree of locality (or window size) dependent on the array (VNIR or SWIR), the land cover, the environmental conditions and the application. The consistency of the size of window used in the local destriping algorithm needs to be studied further. It seems

likely that the window used for data acquired by the VNIR array will normally be much smaller than that used for data acquired by the SWIR array. This is a function of the different noise patterns in data resulting from the two arrays.

It seems that the current standard and advanced atmospheric correction methods provide useful normalizations of the data and can certainly be recommended for consistent analysis of time series such as that of the CIAS. However, it is clear from the work reported here that there will normally be significant (and generally increased) levels of residual noise in the data after any atmospheric correction with consequent reduction in SNR if it is based on current Level 1B1 data. For this reason, extra data cleaning and feature selection was performed and will need to be performed by all users of the data. It also appears that most of the options for noise management are best applied after atmospheric correction. Local destriping is an exception.

This paper has not specifically addressed issues that are currently at the forefront of discussions surrounding atmospheric correction of Hyperion. These include issues such as spectral "smile" effects [33] and adequacy of transmittance codes. We have rather selected a very standard baseline for correction. It is quite likely that there will be added levels of noise reduction from advances in this area in the near future and that these will include more sophisticated handling of the spectral "smile." However, it seems from the investigation in Section VI-A that the indexes being used in this paper (with the possible exception of the dRE) can be used successfully without such further advances.

In summary, the best noise management strategy found here was based on calibrated, locally destriped and atmospherically corrected data. Following this, MNF smoothing was used based on separate MNF transformations of the stable bands of the VNIR and SWIR data followed by inverse transformations retaining only the high MNFs with significant land surface information. The steps we have described can provide an effective processing pathway to generate indexes from apparent surface reflectance images for the time series of EO-1 data that has been acquired for the CIAS. Because the data can be closely related to ground-based hyperspectral data, the standardization allows monitoring and measurement of crop growth from a space platform based on field-scale calibration. The aim is to assess changes in plant chemistry, including changes in nitrogen levels such as those developed for forests in [32], and to model crop yields.

ACKNOWLEDGMENT

The Hyperion data were processed by TRW and provided by NASA. B. Holben (AERONET Group) provided the CIMEL installation. Thanks to M. Bramston, A. Tiwari, R. Robinson, and G. Robertson (Coleambally Irrigation Cooperative Limited) and the landholders for their cooperation and support, G. Beecher and B. Dunn (NSW Department of Agriculture) for their real-time differential GPS unit, J. Angus (CSIRO) for the SPAD meter, D. Graetz (CSIRO) for field equipment. Particular acknowledgment is due to J. Lovell, S. Campbell, and E. King for computing and field support and the Mineral Mapping and Technology Group of CSIRO for access to their MMTG-A set of software.

REFERENCES

[1] J. Pearlman, S. Carman, C. Segal, P. Jarecke, and P. Barry, "Overview of the Hyperion imaging spectrometer for the NASA EO-1 mission," in *Proc. IGARSS*, Sydney, Australia, 2001.

[2] S. G. Ungar, "Overview of EO-1, the first 120 days," in *Proc. IGARSS*, Sydney, Australia, 2001.

[3] M. S. Moran, Y. Inoue, and E. M. Barnes, "Opportunities and limitations for image-based remote sensing in precision crop management," *Remote Sens. Environ.*, vol. 61, pp. 319–346, 1997.

[4] P. L. Nagler, C. S. T. Daughtry, and S. N. Goward, "Plant litter and soil reflectance," *Remote Sens. Environ.*, vol. 71, pp. 207–215, 2000.

[5] E. Boeg, H. Soegaard, N. Broge, C. B. Hasager, N. O. Jensen, K. Schelde, and A. Thomsen, "Airborne multispectral data for quantifying leaf area index, nitrogen concentration, and photosynthetic efficiency in agriculture," *Remote Sens. Environ.*, vol. 81, pp. 179–193, 2002.

[6] I. B. Strachan, E. Pattey, and J. B. Biosvert, "Impact of nitrogen and environmental conditions on corn as detected by hyperspectral reflectance," *Remote Sens. Environ.*, vol. 80, pp. 213–224, 2002.

[7] M. E. Martin and J. D. Aber, "High spectral resolution remote sensing of forest canopy lignin, nitrogen, and ecosystem processes," *Ecol. Appl.*, vol. 7, pp. 431–443, 1997.

[8] D. N. H. Horler, M. Dockray, and J. Barber, "The red edge of plant leaf reflectance," *Int. J. Remote Sens.*, vol. 4, pp. 273–288, 1983.

[9] P. J. Curran, J. L. Dungan, B. A. Macler, and S. E. Plummer, "The effect of a red leaf pigment on the relationship between red edge and chlorophyll concentration," *Remote Sens. Environ.*, vol. 35, pp. 69–76, 1991.

[10] A. A. Gitelson, M. N. Merzlyak, and H. K. Lichtenthaler, "Detection of red edge position and chlorophyll content by reflectance measurements near 700 nm," *J. Plant Physiol.*, vol. 148, pp. 501–508, 1996.

[11] I. Filella and J. Peñuelas, "The red edge position and shape as indicators of plant chlorophyll content, biomass, and hydric status," *Int. J. Remote Sens.*, vol. 15, pp. 1459–1470, 1994.

[12] Z. Chen, C. D. Elvidge, and W. T. Jansen, "Description of derivative-based high spectral-resolution (AVIRIS) green vegetation index," *Proc. SPIE*, vol. 1937, pp. 43–54, 1993.

[13] C. D. Elvidge and Z. Chen, "Comparison of broad-band and narrow-band red and near-infrared vegetation indices," *Remote Sens. Environ.*, vol. 54, pp. 38–48, 1995.

[14] B. Datt, "A new reflectance index for remote sensing of chlorophyll content in higher plants: Tests using Eucalyptus leaves," *J. Plant Physiol.*, vol. 154, pp. 30–36, 1999.

[15] J. Peñuelas, J. Piñol, R. Ogaya, and I. Filella, "Estimation of plant water concentration by the reflectance water index WI (R900/R970)," *Int. J. Remote Sens.*, vol. 18, pp. 2869–2875, 1997.

[16] B. C. Gao, "NDWI—A normalized difference water index for remote sensing of vegetation liquid water from space," *Remote Sens. Environ.*, vol. 58, pp. 257–266, 1996.

[17] G. P. Asner and D. B. Lobell, "A biogeophysical approach for automated SWIR unmixing of soils and vegetation," *Remote Sens. Environ.*, vol. 74, pp. 99–112, 2000.

[18] R. N. Clark and T. L. Roush, "Reflectance spectroscopy: Quantitative analysis techniques for remote sensing applications," *J. Geophys. Res.*, vol. 89, pp. 6329–6340, 1984.

[19] R. N. Clark, T. V. V. King, M. Klejwa, G. Swayze, and N. Vergo, "High spectral resolution reflectance spectroscopy of minerals," *J. Geophys.Res.*, vol. 95, pp. 12 653–12 680, 1990.

[20] R. N. Clark, G. A. Swayze, A. Gallagher, N. Gorelick, and F. Kruse, "Mapping with imaging spectrometer data using the complete band shape least-squares algorithm simultaneously fit to multiple spectral features from multiple materials," in *Proc. 3rd Airborne Visible/Infrared Imaging Spectrometer (AVIRIS) Workshop*, 1991, JPL Pub. 91–28, pp. 2–3.

[21] B. N. Holben, T. F. Eck, I. Slutsker, D. Tanre, J. P. Buis, A. Setzer, E. Vermote, J. A. Reagan, Y. J. Kaufman, T. Nakajima, F. Lavenu, I. Jankowiak, and A. Smirnov, "AERONET—A federated instrument network and data archive for aerosol characterization," *Remote Sens. Environ.*, vol. 66, pp. 1–16, 1998.

[22] R. M. Mitchell and B. W. Forgan, "Aerosol measurements in the Australian outback: Intercomparison of sun photometers," *J. Atmos. Oceanic Technol.*, vol. 20, pp. 54–66, 2003.

[23] T. R. McVicar, T. G. Van Niel, and D. L. B. Jupp, "Geometric validation of Hyperion data acquired by Earth Observing 1 satellite at Coleambally Irrigation Area," Commonwealth Scientific and Industrial Research Organization, Canberra, Australia, CSIRO Land and Water Tech. Rep. 46/01, 2001.

[24] A. A. Green, M. Berman, P. Switzer, and M. D. Craig, "A transformation for ordering multispectral data in terms of image quality with implications for noise removal," *IEEE Trans. Geosci. Remote Sensing*, vol. 26, pp. 65–74, Jan. 1988.
[25] A. F. H. Goetz, Z. Qu, B. Kindel, and M. Ferri, "Atmospheric correction of Hyperion data and techniques for dynamic scene correction," in *Proc. IGARSS*, vol. III, Toronto, ON, Canada, 2002, pp. 1408–1410.
[26] T. W. Cooley, G. Anderson, G. W. Felde, M. L. Hoke, and A. J. Ratkowski, "FLAASH, A MODTRAN-4 based atmospheric correction algorithm, its application and validation," in *Proc. IGARSS*, vol. III, Toronto, ON, Canada, 2002, pp. 1414–1418.
[27] P. Barry, *EO-1/Hyperion Science Data User's Guide*. Redondo Beach, CA: TRW Space, Defense & Inform. Syst., 2001.
[28] T. Cocks, R. Jenssen, A. Stewart, I. Wilson, and T. Shields, "The HyMap airborne hyperspectral sensor: The system, calibration and performance," in *Proc. 1st EARSEL Workshop on Imaging Spectroscopy*, Zurich, Switzerland, Oct. 1998, pp. 37–42.
[29] B. K. P. Horn and R. J. Woodham, "Destriping landsat MSS images by histograms modification," *Comput. Graphics Image Process.*, vol. 10, p. 69, 1979.
[30] K. G. Joreskog, J. E. Klovan, and R. A. Reyment, *Geological Factor Analysis*. Amsterdam, The Netherlands: Elsevier, 1976, p. 178.
[31] J. W. Boardman, "Post-ATREM polishing of AVIRIS apparent reflectance data using EFFORT: A Lesson in accuracy versus precision," in *Summaries of the 7th JPL Airborne Earth Science Workshop*, vol. 1, 1998, JPL Pub. 97–21, p. 53.
[32] N. C. Coops, M. L. Smith, M. E. Martin, S. V. Ollinger, and A. A. Held, "Predicting Eucalypt biochemistry from HYPERION and HYMAP imagery," in *Proc. IGARSS*, Toronto, ON, Canada, 2002.
[33] D. L. B. Jupp, B. Datt, T. R. McVicar, T. G. Van Niel, J. S. Pearlman, J. Lovell, and E. G. King, "Improving the analysis of Hyperion red edge index from an agricultural area," in *Proc. SPIE Conf. Remote Sensing Asia 2002*, Hangzhou, China, Oct. 2002.
[34] A. F. H. Goetz, G. Vane, J. Solomon, and B. N. Rock, "Imaging spectrometry for Earth remote sensing," *Science*, vol. 228, pp. 1147–1153, 1985.
[35] L. Ong, private communication, 2002.

Bisun Datt received the B.S. degree in physics and mathematics, the PG Dipl. in physics, and the M.S. degree in physics from the University of the South Pacific, Suva, Fiji, in 1985, 1992, and 1996, respectively. He received the Ph.D. degree in remote sensing from the University of New South Wales, Sydney, Australia, in 1999.

He is currently with the Commonwealth Scientific and Industrial Research Organization Earth Observation Centre, Canberra, Australia. His main research interests are in hyperspectral remote sensing of vegetation and soils with specific applications in agricultural crops and forest biochemistry. He is a Co-Investigator for the EO-1 Hyperion calibration/validation activities in Australia, through Australian membership of NASA's EO-1 Science Validation Team.

Tim R. McVicar received the B.S. (honors I) from the University of Queensland, Brisbane, Australia, and the Ph.D. degree from the Australian National University, Canberra, Australia, in 1988 and 2001, respectively.

In 1989, he joined the Division of Water Resources, Commonwealth Scientific and Industrial Research Organization (CSIRO) Land and Water, Canberra, Australia. He is currently a Senior Research Scientist in the Integrated Catchment Management Research Directorate with CSIRO Land and Water, and is a Co-Investigator for the Australian team of the National Aeronautics and Space Administration's EO-1 Science Validation Team. His research interests include time series remote sensing for ecohydrological and agricultural applications.

Tom G. Van Niel received the A.A.S. degree from Monroe Community College, Rochester, NY, and the B.S. and M.S. degrees from Utah State University, Logan.

He is currently an Experimental Scientist with the Integrated Catchment Management Research Directorate, Commonwealth Scientific and Industrial Research Organization Land and Water, Canberra, Australia and is involved in the Measurement and Mapping Program for the Cooperative Research Centre for Sustainable Rice Production, Wagga Wagga, Australia. His research interests are in spatio-temporal analysis as well as error and uncertainty of spatial data.

David L. B. Jupp (A'90) received the B.S. degree from Adelaide University, Adelaide, Australia, and the Ph.D. degree from Flinders University, Adelaide, Australia, in 1969 and 1973, respectively.

He is currently with the Commonwealth Scientific and Industrial Research Organization Earth Observation Centre, Canberra, Australia. His areas of interest have included scene and image modeling, BRDF modeling, hyperspectral data analysis, applications, technology transfer, and commercialization of remote sensing. Applications include coastal zone and inland waters, water resources applications, land surface temperature for applications to soil moisture, and water balance estimation. International collaboration has included work with groups in the United States, Southeast Asia, and China. He is Principal Investigator for the Australian membership of the National Aeronautics and Space Administration EO-1 Science Validation Team.

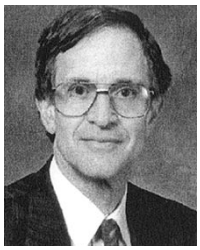

Jay S. Pearlman (M'84–SM'03) received the B.S. degree from the the California Institute of Technology, Pasadena, and the Ph.D. degree from University of Washington, Seattle.

He is currently the Chief of Science and Applications for the Advanced Network Centric Operations, Phantom Works, Boeing Company, Seattle, WA, and is actively involved in remote sensing development and applications. Previously, he was with TRW, Redondo Beach, CA, and was Deputy Program Manager and Scientist for the Hyperion instrument on EO-1. In addition to instrument development, his activities include applications of remote sensing to agriculture and forestry using both airborne and space-based systems.

Dr. Pearlman is an Associate Editor of the IEEE TRANSACTIONS ON GEOSCIENCE AND REMOTE SENSING.